ISTFA™ 2009, Conference Proceedings from the
35th International Symposium for Testing and Failure Analysis
November 15–19, 2009, San Jose, California, USA, p 149-156

Comparative Failure Analysis of Photovoltaic Devices

Jim Colvin
FA Instruments, Inc.
2381 Zanker Rd. #150
San Jose, CA 95131
(408) 428-9353
E-mail: jim@fainstruments.com

Abstract

Photovoltaic devices (PV) or more commonly "solar cells" are analyzed using LBIC/LBIV (Light Beam Induced Current/Voltage) PL (Photoluminescence) and EL (Electroluminescence) as well as INSB thermal Methods. This paper will show the advantages and pitfalls of the techniques as well as a novel way to perform EL imaging without a dark box and thermal imaging through glass panels.

Introduction

Photovoltaic cells are effectively large area diodes with metal electrodes spaced to minimize the loss of fill factor from the light. Popular cell materials are: Silicon, Cadmium Telluride, Copper Indium Selenide, GaAs, Light absorbing dyes (DSSC) and Organic/polymer based cells. [1] Since these cells are covered only minimally by metal, EL imaging can be performed on both crystalline and amorphous versions of the cells. Certain specialized organic thin film cells may not generate an EL or PL signal and can only be mapped thermally to look for ohmic shorts or map the interconnections while biased. LBIC is useful as the local conversion efficiency of the thin film can be mapped but near bandgap light must be used for subsurface defect detection and mapping in the presence of significant shunt resistance may be difficult. Normal (LSM) Laser Scan Microscopes are not very useful, as large areas cannot be readily mapped and the power varies dependent on the scan angle through the optics. The solution is to raster the laser using SIFT (Stimulus Induced Fault Test)[2,3] The SIFT scanner is a large area X, Y, Z positioner that allows the laser to be rastered and positioned over a large area similar to an engraving machine. Since the spot is at a constant location internal to the optics, the power is also constant. Tilt is compensated in all three axes to insure constant power distribution with a constant spot size. This is especially important with laser excited PL imaging and thermal laser injection methods. The raster, spot size, and scan rate are controlled to produce an LBIC or TLS (Thermal Laser Stimulus) scan of the array in a similar but larger scale to OBIRCH or TIVA methods.[4,5]

Sensor and System Considerations

The 3 most common imaging sensors for analysis of photovoltaic technology for EL and PL techniques are Si CCD, MCT and InGaAs. Figure 1 compares typical response characteristics in relation to Si in order to show the small overlap enabling CCD sensors to be used for EL imaging. Note the Depletion CCD reaches into the active indirect bandgap region of Si at 1.1 eV or around the 1000nm to 1100nm region. Clearly for EL and PL imaging, the InGaAs or MerCad (MCT) cameras are superior from a performance perspective however the price differential favors CCD as the low cost solution. Typical performance differences place the InGaAs at 60 times more sensitive than CCD making CCD a poor choice for PL imaging, whereas EL imaging is acceptable using longer integration times. Sensor resolution must not be dismissed. Higher resolution is not necessarily better. The system must be matched to the capabilities of the optics in the system. The optics define ultimate resolving power, whereas the sensor array size dictates field of view, NOT resolution. Sensitivity and resolution are inversely proportional. A 500x500 pixel array is 4 times more sensitive than a 1000x1000 pixel array. The light is further subdivided amongst a higher pixel count decreasing sensitivity. This fact is often overlooked resulting in the purchase of megapixel cameras that perform poorly.

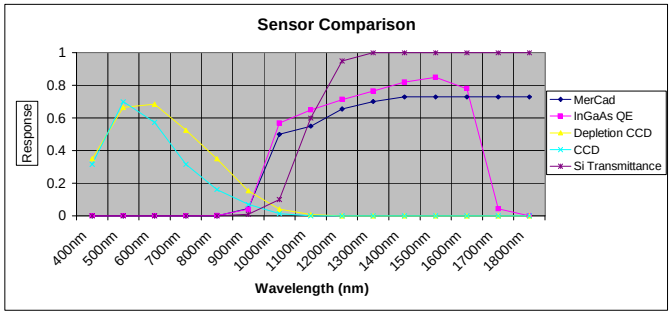

Figure 1. Graph of typical sensor spectral response for CCD, MCT and InGaAs cameras.

Two typical setups are shown for plan view imaging. Figure 2 is a probe station setup on a vibration isolation table with CCD, InGaAs, and SIFT laser scan capabilities. This type setup is useful for analyzing individual cells and smaller modules especially where the electrical connections are missing or require probing. Figure 3 operates from the same control platform with the camera head and interchangeable lenses attached to a portable stand. The stand is motorized for precise control of all 3 axes and can do SIFT scans. This portable configuration can rest on top of a solar panel for close inspection work. The entire microscope head can be mounted on this stand to perform similar work to the probe station but without the benefit of vibration isolation. Dark box environments can be achieved by draping a light blocking

cloth around the setup or using stabilized differential methods described later in the paper. A third configuration is to use a standard tripod for camera positioning.

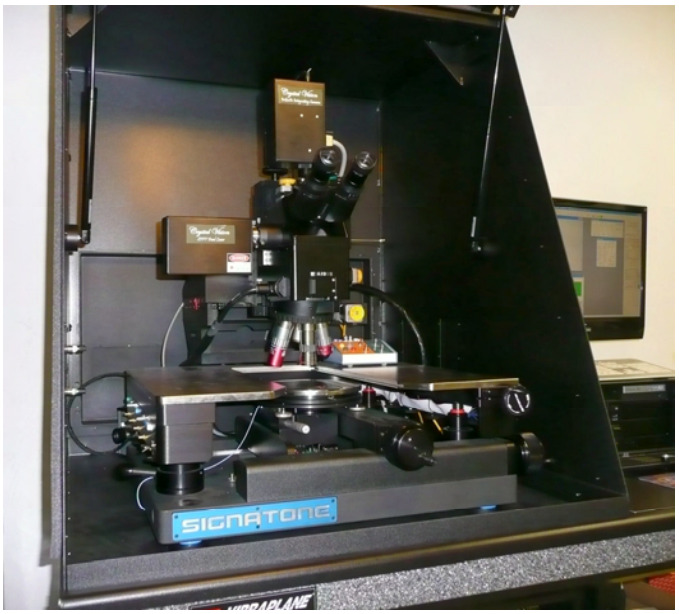

Fig 2. Probe station equipped with InGaAs integrating camera and scanning laser sources for LBIC and Thermal stimulus.

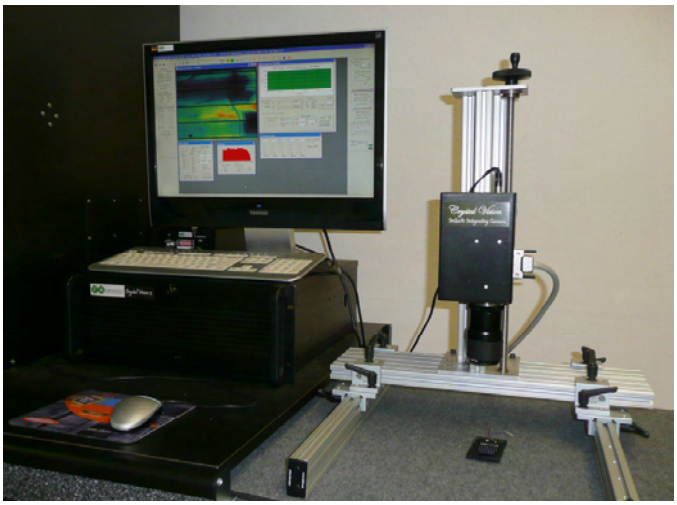

Fig 3. Portable InGaAs system for cell, module and panel inspection.

Basic Electroluminescence Imaging

Electroluminescence occurs when current flows across a forward biased diode. When the minority carriers recombine, photons are emitted with an energy of 1.1 eV (silicon). The resulting light from the activity of the minority carriers can be collected and imaged. A light emitting diode (LED) is an efficient EL device whereas silicon is not, due to the indirect bandgap. Radiative recombination of electrons and holes is a low probability event due to the large mismatch of momentum between the available electron and hole states. In spite of the inefficiency, EL signals are obtainable with integrating CCD or InGaAs type cameras. Areas where the field is reduced such as proximal to a shunt or a resistive to open interconnect will result in a corresponding reduction in the EL signal as will surface trap sites (Dangling bonds, contamination, or other lattice defects). The cell or module is biased forward to force current flow through the cell or module. The chosen bias is dependent on the desired effect. For the monocrystalline Si cell in figures 4 and 5, a crack is easily identified that is not seen with visible illumination, the arrows additionally show local areas of missing backside contact to the anode and the top metal finger shows a greatly reduced EL signal for figures 5 and 7. Figure 6 is a magnified view of the scratch resulting in a discontinuity. Note the reduced EL signal along the length of the top finger in figures 4-6.

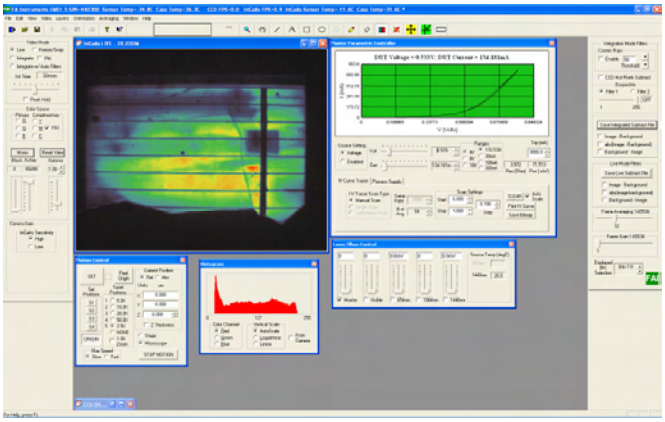

Fig. 4. Screen shot of InGaAs image with curve for a crystalline photovoltaic. The Photovoltaic has a vertical crack as well as a discontinuity in the upper horizontal finger.

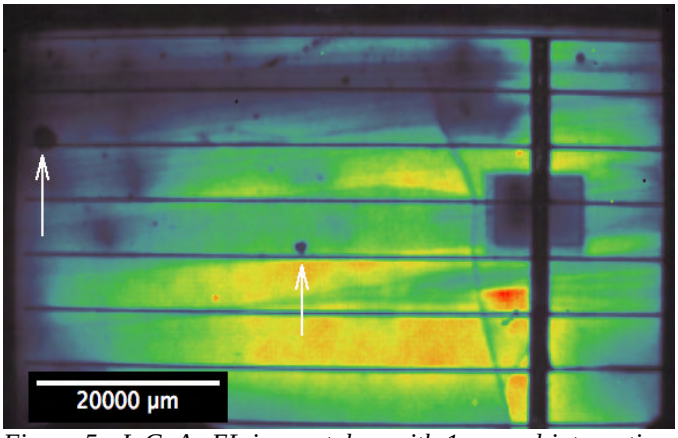

Figure 5. InGaAs EL image taken with 1 second integration. The cell drive current is 50mA. The arrows show local areas of missing backside anode contact. The top finger has a reduced EL signal due to a discontinuity in the metal finger.

Although the identified crack does not show with visible light, it is easily seen when illuminated in the NIR spectrum. Figure 8 illustrates the effect of illumination off axis (darkfield). Since Si is relatively transparent at 1064nm, the crack can easily be observed without bias.[6]

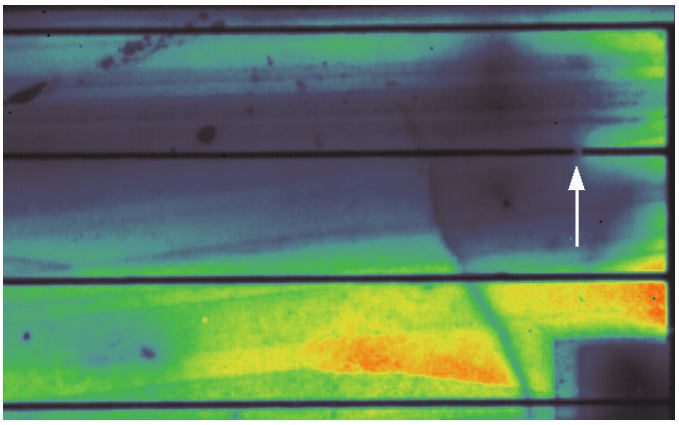

Figure 6. Location of scratched cathode finger on the surface of the cell.

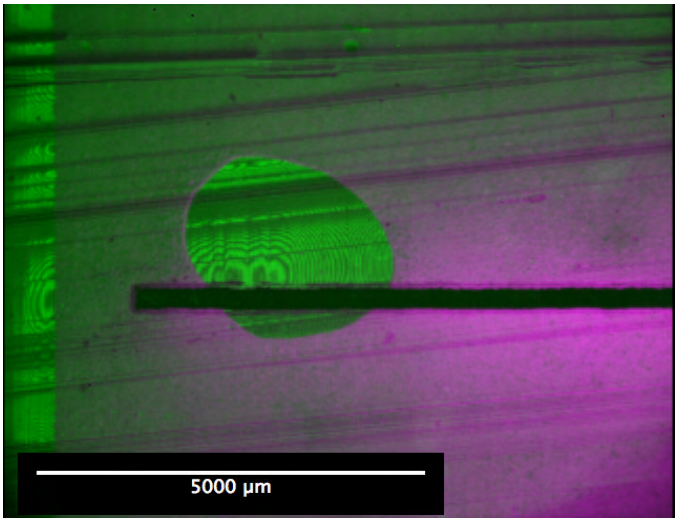

Fig. 7: The EL image of dark circle on the left center side of fig 5 is shown magnified here. The EL image is reduced within this zone due to a locally etched backside electrode during processing. The increased resistance results in less recombination in the "hole".

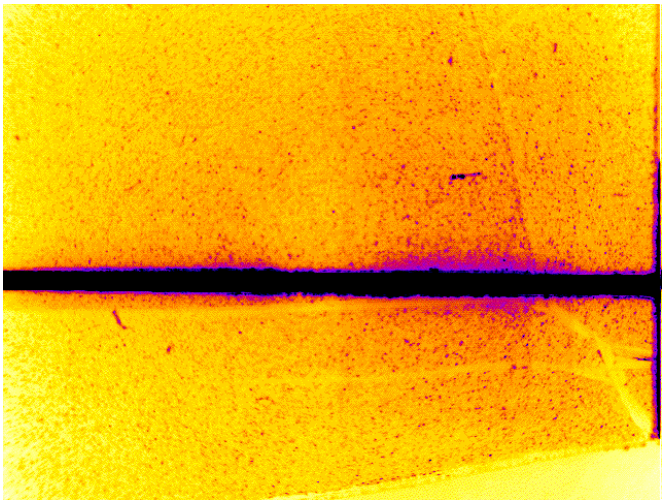

Fig. 8. Portion of the vertical crack imaged with a ringlight at 1064nm to enhance.

Light Beam Induced Current/Light Beam Induced Voltage

The setup to obtain an LBIC/LBIV (also known as OBIC: Optical Beam Induced Current) image using SIFT will allow a comparison and facilitate an explanation of the scanner. The SIFT scanner does not use traditional laser scanning microscope optics. DUT scan area can be submicron to 7" or more, allowing large areas to be analyzed since the scanners are stepper-based rather than internal optics based. Field of view limitations of objectives on LSM (Laser Scan Microscope) based equipment are eliminated with SIFT as are issues with varying beam power across the raster. The system can be based on either a motorized probe station or microscope stand for field applications. Unlike LSMs, SIFT uses a stationary beam and moves either the stage or the microscope head in a raster scan pattern. Figure 9 is a block diagram of the apparatus. A microscope and stage are equipped with stepper motors to control the X, Y, and Z motion of the scan. Obviously, servo motors or similar linear positioning devices can be used in place of stepper motors. Z control is necessary to control the spot size of the stimulus by focal point methods. Laser based SIFT uses a laser attached to one of the beam ports of the microscope and can be any wavelength compatible with the selected optics. The selected objective, aperture, and focus control spot size.

The microcontroller handles X-Y-Z positioning, stimulus, sensor feedback and communicates with the tester. The controller also optionally manages the bias circuit. Scans are initiated by selecting start and end corners and the step interval for the scan. The smaller the step interval, the greater the resolution of the scan generated mage. Laser spot size is managed by the diffraction limit of the selected objective in conjunction with the focus. Scan time is then calculated as the total number of steps multiplied by the step delay (settle time).

As a side note, gas CO_2 lasers can be mounted in place of the microscope (glass optics are not compatible) and raster scanned over large areas for thermal SIFT. CO_2 lasers are chosen due to low cost, power and desired wavelength for thermal stimulus. The laser does not generate recombination in common photovoltaic materials and is a long enough wavelength (low energy photons) to be more readily absorbed by the substrate than the more traditionally used 1340nm laser for silicon. The change in resistance, voltage, or current of the cell, as desired, is monitored during the scan and overlaid with the reflected image. Thermal laser mapping is beyond the scope of this paper but is mentioned here for follow on work in relation to the SIFT scanner description.

The stimulus can also be introduced over the DUT with the raster applied to the stage. This method of SIFT can be thought of in the same way a probe is positioned over a DUT by moving the stage.

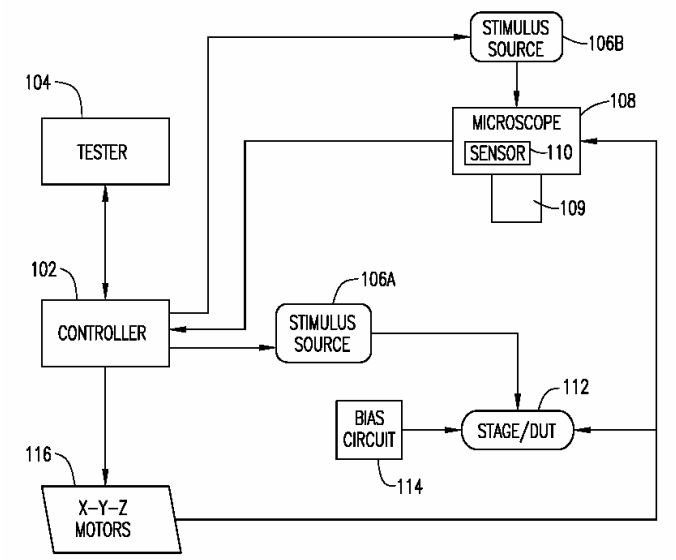

Figure 9. Block Diagram of SIFT Scanner.

Image reconstruction is obtained as the sample is scanned point by point. There are 8 amplifiers available to measure signals such as the reflected laser signal for the background image formation and the modulated voltage or current signal from the DUT. These signals are superimposed on the reflected signal data, if desired, during the scan. Typically LBIC is a measure of the small signal voltage developed across a resistor tied between the anode and cathode of a cell. The value of the resistor needs to be large and properly chosen. In many instances the cell leakage is considered the resistor and the developed voltage is measured directly at the terminals with a high impedance amplifier (LBIV). This has the advantage of providing shunt leakage information from series wired cells. Compare the LBIC signal in figure 10 to the EL data obtained in figures 4-7. Note the crack is the only surface anomaly shown at the 654nm wavelength.

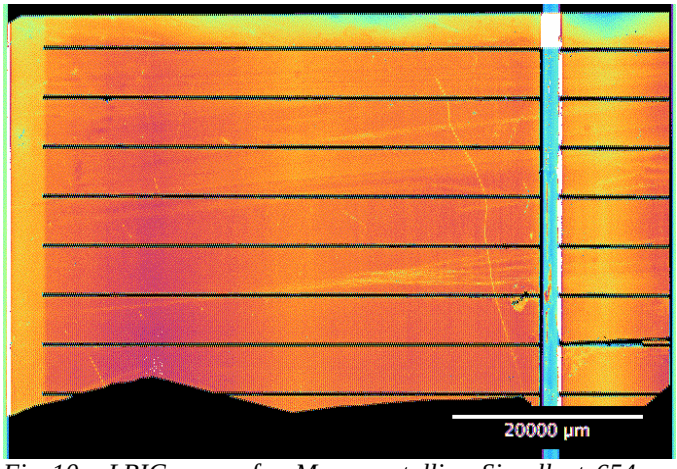

Fig 10. LBIC scan of a Monocrystalline Si cell at 654nm. Note the crack running up the cell above the micron scale bar, the other subsurface anomalies are not revealed from figure 5.

An amorphous Si panel on a glass substrate was investigated with EL and LBIV methods. EL imaging revealed anomalies with the backside electrode in figure 11. The LBIV scan shows the actual cell-to-cell local conversion efficiencies as shown in figure 12. Figure 13 is an averaged line plot profile from figure 12. When performing LBIV on series cells, the impedance load is of a rather high impedance, otherwise the adjacent series cells will reverse bias. Under these conditions, any local leakage within the specific cell in the chain will reduce the signal and as such serves as the built in shunt for the LBIV signal. With a high impedance measurement, all other cells will appear as a short, since the measured voltage associates only with the cell being stimulated. If an external resistive shunt is used, the cells must be connected individually rather than in series for LBIC mode.

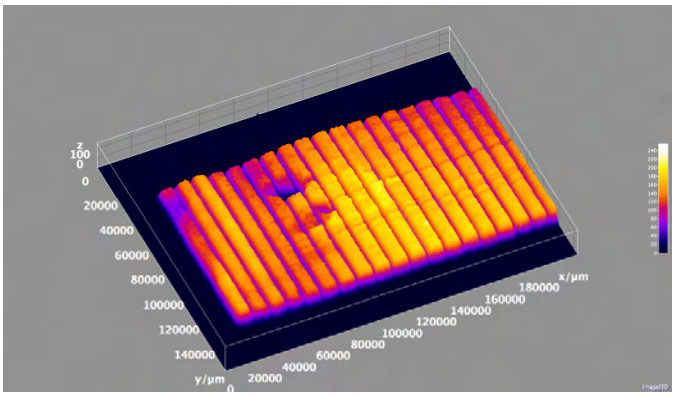

Fig. 11. EL image of a forward biased amorphous Si panel at 22V and 8mA of forward current. Note the holes in the signal near the center due to backside electrode disparities. Compare to the LBIV image in figure 12.

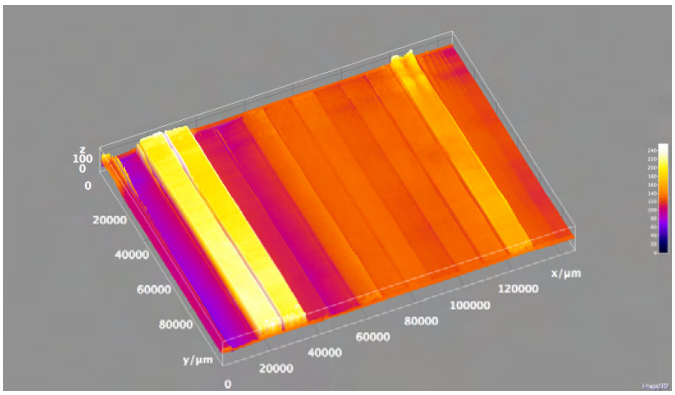

Fig. 12. Large area LBIV scan of an amorphous silicon module on glass photovoltaic. The LBIC signal reveals the cells with the best conversion efficiency and highlights local surface disparities. Backside contact issues are not revealed.

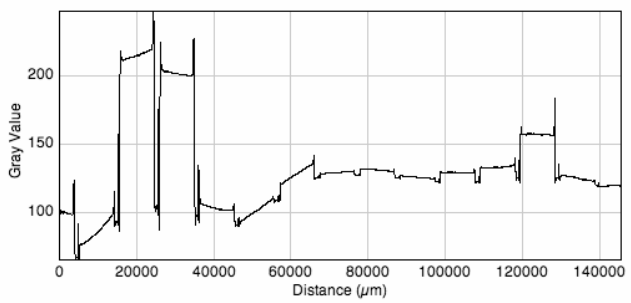

Figure 13. Profile graph from figure 12 of a large area LBIV scan on an amorphous silicon module on glass photovoltaic. The LBIV plot reveals the cells with the best conversion efficiency.

Stabilized Luminescent and Thermal Imaging

Traditional thermal imaging methods typically utilize a background reference image with no bias, and then a subsequent biased image is acquired and compared. The length of time to acquire is typically seconds, resulting in thermal propagation across the cell during signal acquisition diluting a useful result. Using stabilized mode, sensitivity will be shown to be far superior to IR camera imaging methods and does not suffer the sqrt(2) noise increase and hence 2X amplitude loss inherent in lock in thermography systems (LIT). [7,8]

This method of acquisition controls synchronously to the camera frame rate the thermal propagation, (stabilizes the substrate temperature with interleaved bias pulses) while building up the thermal signal to enhance the thermal sensitivity. This work was originally published for Moiré pattern thermal mapping. [9]

Referring to equation (1) the difference signal is built up using a summed sequence of frames from state 1 and state 0. For Stabilize 1x, the Device Under Tests (DUT) alternates between States 1 and 0 for every frame. For Stabilize 2x, the DUT alternates between States 1 and 0 every 2 frames, and so on. Stabilize can run any binary multiple. The absolute value is used as a "catch all" for both 0 and 180 phase situations. Thermal shifts increasing or decreasing are mapped but the polarity is, of course, lost. The flags controlling absolute value and polarity: (state 1 sum – state 0 sum) or (state 0 sum – state 1 sum) can be toggled during acquisition to force a recalculate and display.

Equation (1)

$$\text{Frame} = \left| \sum_{n=0}^{N/2} (\text{State 1 Frames}) - \sum_{n=0}^{N/2} (\text{State 0 Frames}) \right|$$

Using Stabilize 4x as an example, at 30 frames/second it becomes apparent that the thermal propagation will be 4/30 second on and 4/30 second off for a cycle time of 3.75 Hz. The frame groups of on and off (State 1 and State 0) are accumulated in an interlaced fashion and displayed to allow the analyst to watch the signal grow and to stop the acquisition at sufficient intensity. The end result will be N accumulated frames in packets of 4. The interface can trigger with a test sequence in slave mode or drive the modulated power directly to the device. This stabilize method of acquisition is also compatible with FMI (Fluorescence Microthermal Imaging). The ability to visualize and control the propagation per unit time gives insight as to the location and nature of the defect and its surroundings.

A normal polycrystalline cell was investigated to demonstrate the sensitivity of the technique for figures 14-17. Compare the EL image in figure 14 to the high gain thermal image in forward and reverse bias for figure 16. The 2 spots in the center are diffusion anomalies based on their presence restricted to forward bias modes. The PL image, in figure 17, was obtained using a 670nm excitation source with the InGaAs camera and a longpass filter close to the bandgap of silicon to reject the 670nm signal component to the camera. Note the similarities to the EL signal from figure 14. PL data yields information on the minority carrier lifetime. Trap sites such as dangling bonds are revealed with PL imaging. Experimental material without electrodes can be evaluated with PL since the "bias" is the high-energy photon beam impinging on the surface generating hole electron pairs and subsequently recombination at the bandgap of the material studied. The n or p material can be examined individually during process development making PL a powerful process development/monitor technique.

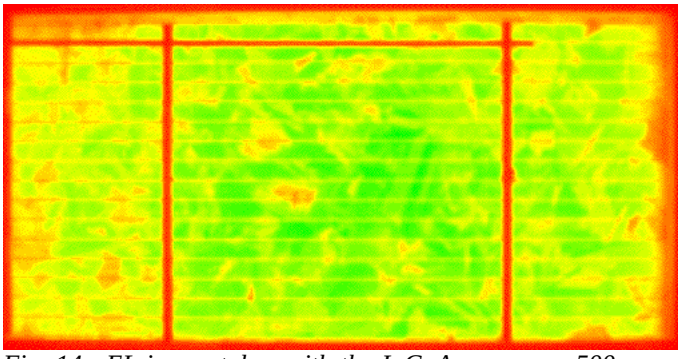

Fig. 14. EL image taken with the InGaAs camera. 500msec. at 200mA drive current.

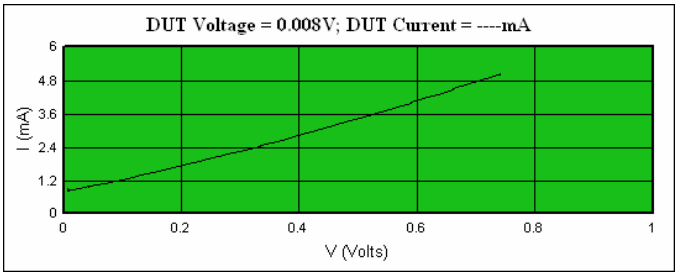

Figure15. Curve in reverse bias mode to identify low-level hot spots using the InSb camera in stabilized thermal mode. See figure 16.

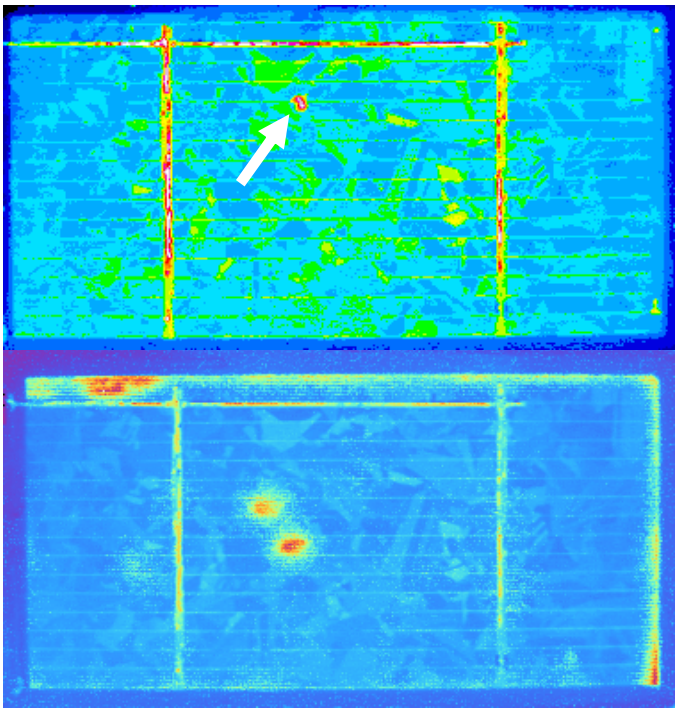

Figure16. INSB thermal images of a typical cell with 1024 frames and 256 gain at 3.75 Hz modulation (4X Stabilize). Upper Image is Reverse bias at 734mv and 5ma. Lower image is forward bias 735ma at 352ma. The shunt is weak in the enhanced upper image.

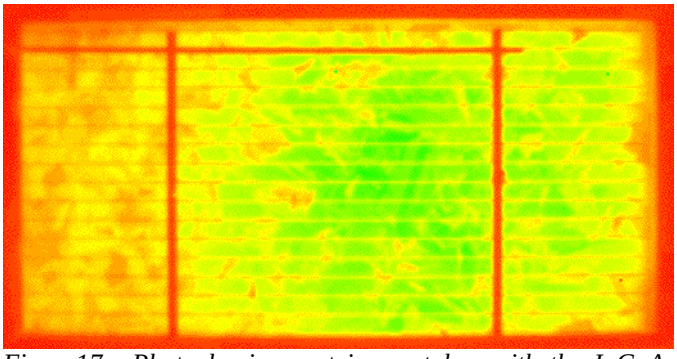

Figure17. Photo luminescent image taken with the InGaAs camera using a flood source of 670nm to irradiate the surface of the unbiased cell. A longpass filter was used to minimize leakage. Note the similarity to the EL image in figure 14.

Large area solar panel analysis

One of several challenges with EL and thermal imaging is the size of the area to be investigated. A dark box is not necessarily practical for solar panels. The stabilized luminescent method above is implemented using frame acquisition with modulating power to the panel. By capturing frames in alternating on and off states, the background illumination can be differentially removed allowing the remaining EL signal to be viewed and quantified. Since the integration times for the camera are shorter, camera requirements are less stringent since camera defects are differentially removed from the image, a fringe benefit of the technique. The upper limit is based on the S/N of the accumulated camera frames. Typically gains of up to 60X can be realized with typical 12 bit InGaAs cameras.

Shunts can be identified in series/parallel wired panels by imaging at different drive current levels. The panel is an 18x42 inch monocrystalline panel rated at 4 amps and 60 Watts with a Voc of 20V. The panel slipped past production into the field. In figure 18, top image, the panel was imaged at 2A using 1/30 sec integration and a simple background subtract. Note the 2 cells 1 weak and 1 dead at location 4,0 and 4,1 (8 cells across by 9 cells high). The current was reduced further to 1A for the center image. Now the 2 cells at 4,0 and 4,1 are both dead with all the cells above in the same column appearing brighter. The dead cells must have shunts causing greater current to flow in column 4 and less in parallel wired column 3. Note column 3 is indeed darker and location 8,4 is suspect. Reducing the current down to 140 mA in the bottom image the lower level shunt leakages begin to dominate in several areas. The intensity is too low to acquire without increasing the integration time but the sensor will saturate due to ambient light conditions. To solve this, the stabilized mode was used for acquisition with 256 frames and 16 frames per state at 1/30 second integration time.

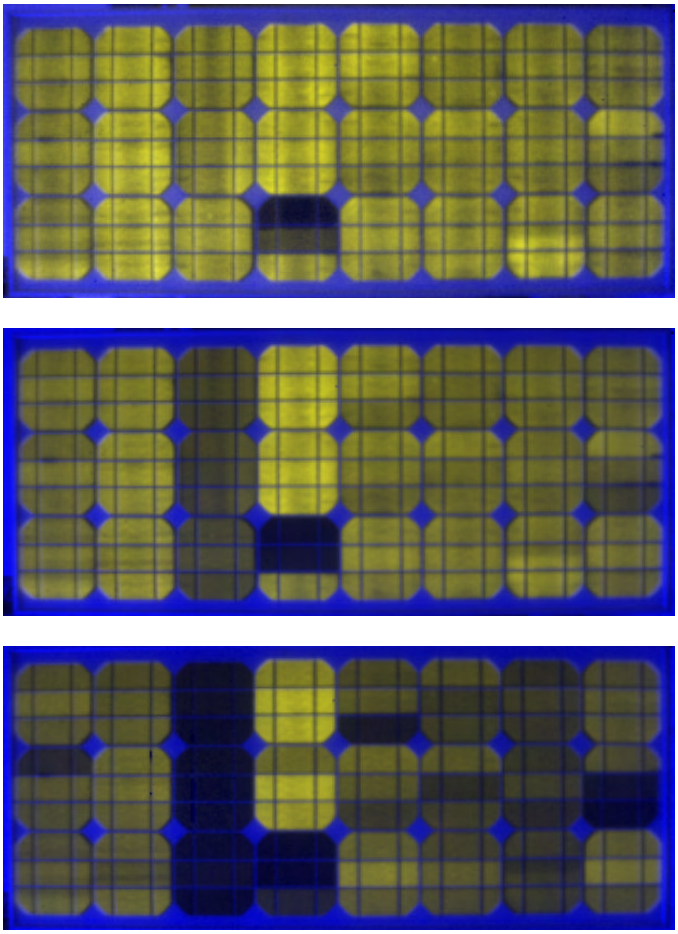

Fig 18. 18x42 inch solar panel InGaAs EL image. Top image is with 2A drive current and 1/30 second integration time. Middle image is with 1A drive current and 1/30 second integration time. Bottom panel is with 140mA drive current and 1/30 second integration time with 256 frames

accumulated in stabilize mode to extract the signal. Each column has 9 cells wired in series. Each column pair is wired in parallel with the parallel pairs wired in series. In EL mode the current will divide between the pairs as becomes evident at 140mA. The middle module from the rightmost column is cracked.

Figure 19. EL image of cracked adjacent cells identified in the rightmost column (8,5) from figure 18. Note the edge shunt leakage on the lower cell from contamination.

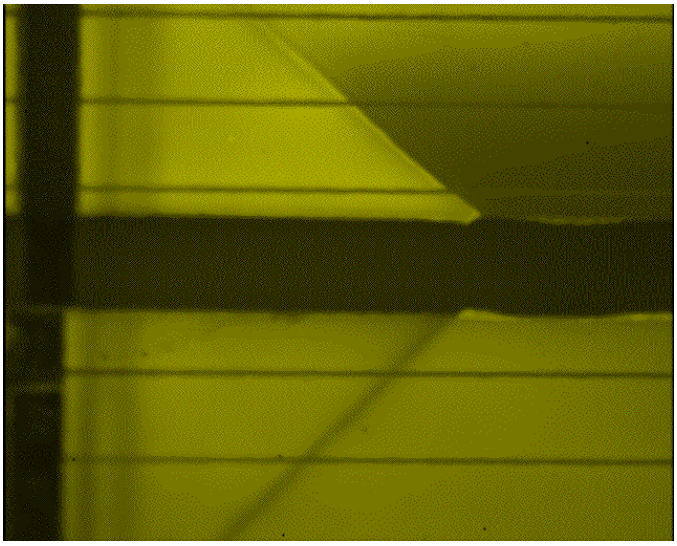

Figure 20. Magnified view of the crack in EL mode from figure 19. Note the mating piece where the crack originates has an irregular cut. The dicing operation is to blame for this failure.

Unfortunately, the original sites in column 4 are not understood at this point and visual inspect is negative for the root cause. The goal is not to destroy the panel until the data is understood. The suspected shunts should show up thermally, as will be shown in the next section.

InSb Investigation of the Solar Panel

The panel was set up and imaged from across the room with the InSb camera on a tripod. The panel is complete with a glass faced window and upon imaging the warm vertical panel, the image in figure 21 was obtained. Not surprising since glass absorbs fairly well in the 3um to 5 um band. Stabilized thermal imaging will not work unless the frame rate is reduced to about 0.1 Hz due to the slow thermal diffusion anticipated through the glass to the surface. In this case, only a differential approach was required based on the strength of the signal, however, stabilized would have been used if warranted. The thermal image is now clear where the shunts are located. The shunt at (8,4) is due to edge contamination as correlated by the EL image in figure 19. Note the crack is not the shunt. The 3 sites at the bottom of column 4 are caused by the series interconnect strap touching the cell edge between the 2 cells.

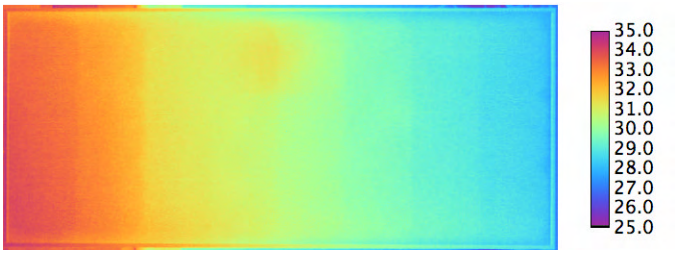

Figure 21. 18x42 inch solar panel imaged with an InSb camera at ambient. The hot end of the panel on the left is actually the top part where heat is rising. Note the cells cannot be seen behind the glass and removal of the glass would be destructive. Units are Celsius.

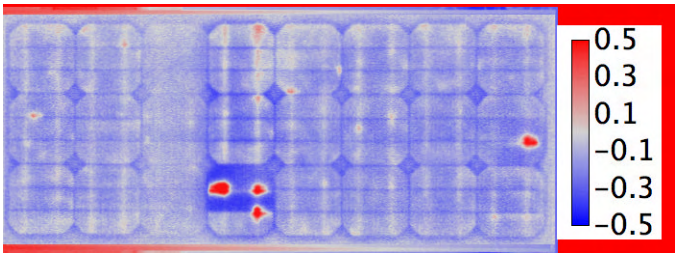

Figure 22 Differential thermal image in degrees C of the 18x42 inch solar panel imaged with an InSb camera after applying 1A for 5 seconds. Compare the identified shunt leakage to Figures 18 and 19. Note the cells can now be "seen" behind the glass since the difference image is being collected on the glass face from heat injected below.

Conclusions

Several case studies of photovoltaic cell and module failures have been shown with emphasis on cross correlation to obtain corrective action. Stabilized imaging has been used to identify low level thermal shunts and has demonstrated how to obtain EL signals without a dark box. Different power levels allow identification/understanding of the nature of the leakage. PL mode can be used to characterize unfinished product. Dopant profiles can be calibrated to the PL signal and minority lifetimes characterized locally. LBIV was shown with constant power, tilt corrected scans on large area panels to

obtain QE surface data. Finally, InSb 3um to 5um imaging technology was demonstrated through glass with differential thermal analysis.

Acknowledgments

To my wife Mayra for her devotion and patience with my continuing to burn the candle at both ends.

References

1. http://www.solarserver.de/wissen/photovoltaik-e.html
2. J. Colvin,"Functional Failure Analysis by Induced Stimulus" ISTFA/2002 Proceedings, pp. 623-630.
3. U.S. Patent # 7323888 B1 "System and Method for Use in Functional Failure Analysis by Induced Stimulus," Colvin; James B.
4. R. Aaron Falk,"Advanced LIVA/TIVA Techniques" ISTFA/2001 Proceedings, pp. 59-65.
5. U.S. Patent # 6,078,183 "Thermally-induced voltage alteration for integrated circuit analysis," Cole, Jr.; Edward I. Sandia Corporation (Albuquerque, NM)
6. J.B. Colvin United States Patent US6134365: Coherent Illumination System and Method.
7 O. Breitenstein, et al, "Fault Localization and Functional Testing of ICs by Lock-in Thermography", Proc. 28th ISTFA, pp. 29-36, 2002.
8. D.L. Barton, "Thermal Defect Detection Techniques", ASM Microelectronic Desk Reference Fifth Edition, pp.378-397, 2004.
9. J. Colvin,"Moire Stabilized Thermal Imaging", IPFA/2005 Proceedings, pp. 163-166.